



The pivot to achieve high current density for biomass electrooxidation: Accelerating the reduction of Ni^{3+} to Ni^{2+}

Zhaohui Yang^{a,1}, Baolong Zhang^{a,1}, Chuanyu Yan^b, Zhimin Xue^{c,*}, Tiancheng Mu^{a,*}

^a Key Laboratory of Advanced Light Conversion Materials and Biophotonics, Department of Chemistry, Renmin University of China, Beijing 100872, China

^b Department of Chemical Engineering and Biomolecular Engineering, National University of Singapore, 4 Engineering Drive 4, 117585, Singapore

^c Beijing Key Laboratory of Lignocellulosic Chemistry, College of Materials Science and Technology, Beijing Forestry University, Beijing 100083, China

ARTICLE INFO

Keywords:

5-hydroxymethylfurfural electrooxidation

Actual current density

Reduction of Ni^{3+} to Ni^{2+}

Rate-determining step

ABSTRACT

Electrochemical oxidation is a promising method to convert 5-hydroxymethylfurfural (HMF) to 2,5-furandicarboxylic acid (FDCA) with high selectivity at room temperature. Developing catalysts with high current densities is crucial for the industrial application of HMF electrooxidation reaction (HMFOR). Herein, we demonstrate that the current densities exhibited by the LSV curves are falsely high and propose to evaluate catalyst activity using anodic peak current density rather than overpotential for the comparison of actual efficiency. Besides, the reduction of Ni^{3+} to Ni^{2+} accompanied by proton coupled electron transfer (PCET) process of HMF dehydrogenation is confirmed as the rate-determining step affecting the conversion efficiency of HMF rather than Ni^{2+} electrooxidation to Ni^{3+} . Theoretical calculations reveal differences in the hydrogen transfer energy barriers of PCET process. Furthermore, $\text{Ni}(\text{OH})_2/\text{NF}$ with appropriate Cr doping shows superb activity with actual current densities of over 230 mA cm^{-2} at HMF concentrations of 10 mM and over 360 mA cm^{-2} at 20 mM (the ever highest current densities for HMFOR), and obtain a yield of more than 98% of FDCA.

1. Introduction

The development and utilization of renewable biomass energy can be a good solution to the current energy and environmental pollution problems [1–4]. As a representative, 2,5-furandicarboxylic acid (FDCA), a typical product of 5-hydroxymethylfurfural (HMF) oxidation, is considered a substitute for petroleum-based terephthalic acid due to its structural similarity, and has promising applications as an important precursor in the production of bio-based plastics, pharmaceuticals, and fine chemicals [5–7]. However, conventional thermal catalytic conversion of HMF to FDCA requires elevated temperatures, noble metal catalysts, and high oxygen or air pressure, which are not in line with the current concept of carbon neutrality and green environment [3,8].

In this regard, electrocatalytic oxidation is a more suitable method as it can convert HMF to FDCA with high efficiency at room temperature and atmospheric pressure, which can replace the traditional conversion method [9–12]. The catalyst covered on the electrode surface is the core of electrocatalytic HMFOR. In recent years, transition metal-based materials such as CoO_xH_y [13], NiSe/NiO_x [14], $\text{MoO}_2\text{-FeP}$ [15], have been developed, among which, Ni-based electrocatalysts are particularly

promising due to the marvelous match between HMFOR and $\text{Ni}^{2+}/\text{Ni}^{3+}$ redox [2,16]. The HMFOR process using Ni-based electrocatalysts can be divided into two steps: Ni^{2+} is oxidized to Ni^{3+} under the action of voltage, which is the electrochemical step; and then is the Ni^{3+} reduction accompanied by spontaneous nucleophilic dehydrogenation of the substrate, which is a non-electrochemical step [16,17]. Previous studies have demonstrated that the dehydrogenation potential of $\text{Ni}(\text{OH})_2$ can be significantly reduced by adjusting the structure or ligand environment [16,18]. The high valence of nickel is more favorable for the adsorption and conversion of HMF when doped with copper, cobalt and other elements, which can effectively regulate the electronic structure of Ni sites and enhance the affinity for the reaction intermediates, thus bringing forward the oxidation potential [2,7,19,20].

How to achieve high electrolytic efficiency under limited mass transfer conditions is still a prerequisite to the industrial application of HMF electrooxidation. Although various catalysts have been reported to exhibit high conversion and Faradaic efficiency [11,21–23], the current density during electrolysis are too low ($< 100 \text{ mA cm}^{-2}$) and the conversion times required are too long to be called high efficiencies. So far, few catalysts have been reported to enable electrolysis at high current

* Corresponding authors.

E-mail addresses: zmxue@bjfu.edu.cn (Z. Xue), tcmu@ruc.edu.cn (T. Mu).

¹ The two authors contribute equally to this manuscript.

densities ($> 200 \text{ mA cm}^{-2}$). More critically, no clear relationship has been established between the catalyst properties and electrolysis efficiency, and there is a lack of unified theoretical basis on how to design catalysts to achieve high current densities, which seriously hinders the research and development of HMF electrooxidation.

Herein, we find that the LSV curves of HMFOR inevitably have an effect of capacitive current due to the presence of scan rate. To extract the effective current density and obtain the maximum conversion efficiency, a segmented *i-t* measurement within the voltage window are proposed to replace the LSV curves. By comparing the actual current densities of X-Ni(OH)₂/CC electrodes (X represents the doped Fe, Co, Mn, Cr, Mo, Ga) in the HMFOR, the results revealed that a lower onset overpotential does not mean that a higher current density can be achieved within the voltage window. This is because the maximum current density under the same mass transfer conditions is strongly dependent on the reduction of Ni³⁺, where the higher the rate of the PCET process of Ni³⁺ reduction coupled HMF dehydrogenation in the non-electrochemical step, the higher the frequency of HMF conversion at active sites. Theoretical calculations confirmed the energy barriers of PCET processes on the X-NiOOH surface and revealed the differences in the corresponding charge densities. Finally, under optimized conditions, Cr-Ni(OH)₂/NF exhibits ultra-fast HMF conversion efficiency, which can completely convert $2 \times 10^{-4} \text{ mol}$ of HMF within 32 min with an over 98% FDCA yield. To the best of our knowledge, this is better than most of the HMF electrocatalysts reported so far. This work not only reports the preparation of high-performance catalysts for HMFOR, but more importantly, provides a unified theoretical guide the design of catalysts that can truly withstand high current densities.

2. Experimental section

2.1. Materials

5-Hydroxymethylfurfural (99%, Aladdin), 2,5-Furandicarboxylic acid (99%, Innochem), 5-formylfuran-2-carboxylic acid (98%, Innochem), 2,5-furandicarboxaldehyde (98%, Innochem), 5-hydroxymethyl-2-furancarboxylic acid (98%, Innochem), potassium hydroxide (95% Macklin), ammonium fluoride (97%, Innochem), urea (99%, Innochem), nickel chloride (98%, Aladdin), cobalt chloride (99%, Innochem), ferric chloride (98%, Aladdin), manganese chloride (99%, Alfa Aesar), sodium molybdate (99%, Macklin), chromium chloride (99%, SCR), Gallium chloride (99.99%, Acros), acetone (99.5%, Acros), ethanol (99.7%, SCR), hydrochloric acid (37%, Innochem), carbon cloth (WOS1009), nickel foam (99.99%, MTI), Milli-Q water (18.2 MΩ) were used without further purification.

2.2. Preparation of electrode

A piece of carbon cloth (CC) ($2 \times 3 \text{ cm}^2$) was first calcined at 500 °C in the air for 4 h, then the CC was cleaned by acetone, 3 M HCl, ethanol and DI water for 15 min, respectively. Taking Co-Ni(OH)₂/CC as an example, a cleaned CC was placed vertically into a 40 mL Teflon-lined autoclave which contained 1.5 mmol NiCl₂·6 H₂O, 0.5 mmol CoCl₂·6 H₂O, 6 mmol CO(NH₂)₂, 2 mmol NH₄F and 30 mL H₂O. Then the autoclave was sealed and heated at 120 °C for 12 h. After reaction, the prepared Co-Ni(OH)₂/CC was taken out and washed three times with water and ethanol. The preparations of carbon cloth supported Mn-Ni(OH)₂, Fe-Ni(OH)₂, Cr-Ni(OH)₂, Mo-Ni(OH)₂, Ga-Ni(OH)₂ are the same as that of Co-Ni(OH)₂ except that CoCl₂·6 H₂O is replaced by MnCl₂·4 H₂O, FeCl₃·6 H₂O, CrCl₃·6 H₂O, GaCl₃ and NaMoO₄·2 H₂O, respectively.

2.3. Electrochemical measurements

The electrochemical performance were measured on a CHI 660E electrochemical workstation with standard three-electrode system consisted of as-prepared electrodes ($1 \times 1 \text{ cm}^2$) as working electrode, a Pt

foil ($1 \times 1 \text{ cm}^2$) and a standard Hg/HgO were used as counter and reference electrode. Five-points activity was tested by applying chronoamperometry at 1.37 V, 1.42 V, 1.47 V, 1.52 V and 1.57 V (vs. RHE), when the current for Ni²⁺ redox drops to 0, HMF is added, the increased is the actual current density of HMF conversion. All tests were performed in H-type cell with Nafion 212 membrane as the separator. Potentials in this study were referred to the reversible hydrogen electrode (RHE) according to the following equation: $E_{\text{RHE}} = E_{\text{Hg/HgO}} + 0.098 + 0.059 \times \text{pH}$. The amount of available active sites was obtained by formula: $n = Q/F$, where Q is the charge of Ni²⁺ oxidized to Ni³⁺ and F is the value of Faraday constant (96,485 C mol⁻¹). Turnover frequency (TOF) was calculated by the equation as $\text{TOF} = j/(6 \times n \times F)$, where j is the current density for HMFOR. *In-situ* Raman was performed on an Xplora Plus Raman instrument with a 10x objective. Raman frequencies were firstly calibrated by Si wafer (520.6 cm⁻¹). A laser power was 1.5 mW and the lines were 633 nm. It took 20 s to obtain one spectrum each time with two accumulations. The electrochemical signal was input through CHI660E, and Ag/AgCl and Pt wire were used as reference electrodes and counter electrodes respectively in the Raman cell.

2.4. HPLC analysis of products

HMF and its oxidation products (HMFA, FFCA, DFF, FDCA) were analyzed by high-performance liquid chromatography (HPLC, LC3000I system with an ultraviolet-visible detector and a 4.6 mm × 250 mm Agilent SB-C18 column). In a typical measurement, a 20 μL aliquot of electrolyte was collected during electrolytic process, diluted to 2 mL with methanol and 5 mM ammonium formate solution (3:7), and then injected into HPLC column for analysis. As for the detecting conditions, the HPLC column temperature was maintained at 35 °C, while the flow rate is 0.6 mL min⁻¹, and the wavelength of UV detection is 265 nm.

The HMF conversion, FDCA selectivity and faradaic efficiency were calculated according to the following equations:

$$\text{HMF conversion}(\%) = \frac{n(\text{consumed HMF})}{n(\text{initial HMF})} \times 100\%$$

$$\text{FDCA selectivity}(\%) = \frac{n(\text{FDCA formed})}{n(\text{HMF consumed})} \times 100\%$$

$$\text{Faradaic efficiency}(\%) = \frac{n(\text{FDCA formed})}{\text{total charge passed} / (6 \times F)} \times 100\%$$

Where F stands for the Faraday constant (96,485 C mol⁻¹).

2.5. DFT calculations

Spin-polarized density functional theory (DFT) method in all computations were performed in Vennie ab-initio simulation package (VASP). The core electrons are described using the projector-augmented-wave (PAW) method, while the Perdew–Burke–Ernzerhof (PBE) functional with in the generalized gradient approximation (GGA) was utilized to treat the electronic exchange-correlation energies. All structures were optimized until the energy and force reached the convergence thresholds of 10⁻⁴ eV and -0.02 eV/Å, respectively. The energy cutoff was set to 450 eV. 20 Å vacuum layer was introduced to ensure enough region to prevent the interaction of adjacent layers. A Monkhorst-Pack k-mesh with a 3 × 3 × 1 k-point grid was used for structural optimization and frequency, while 5 × 5 × 1 for electronic structure calculations.

3. Results and discussion

3.1. The actual current density of HMF electrooxidation

Ni-based materials, represented by $\text{Ni}(\text{OH})_2$, are one of the most promising non-noble metal electrocatalysts for HMFOR [17,24,25]. Previous studies have shown that Ni-based derived materials such as NiP , Ni_3S_2 , etc. also eventually transform to $\text{Ni}(\text{OH})_2$ during the electrooxidation process [26–29]. When $\text{Ni}(\text{OH})_2$ is involved in the anodic reaction, within the voltage window (1.3 ~ 1.6 V vs. RHE), there is a redox current for $\text{Ni}^{2+}/\text{Ni}^{3+}$ transition in the potentiodynamic LSV curves, and the oxidation peak area is strongly dependent on the scan rate (Fig. 1a). As expect, when applied to HMF electrooxidation, the LSV curves also show the correlation with scan rate (Fig. 1b). The higher scan rate, the higher current density that can be achieved, as shown in Fig. 1b, at the scan rate of 10 mV s^{-1} , $\text{Ni}(\text{OH})_2/\text{CC}$ can reach 49.6 mA cm^{-2} at 1.5 V, while at scan rate of 2 mV s^{-1} , only 33.1 mA cm^{-2} can be achieved, which is a great difference. This difference affects the assessment of the actual activity of the Ni-based catalysts. To obtain the actual current densities, segmented five-point chronoamperometry was conducted (Fig. S1a). Unlike the hydrogen evolution (HER) or oxygen evolution (OER) reactions, the catalytic efficiency of HMFOR does not invariably increase with increasing voltage, but rather tends to follow a volcano-shaped curve within the voltage window (Fig. S1b). At lower potentials (< 1.50 V), the current density increases gradually with increasing voltage. After 1.5 V, the current density of HMFOR will decrease due to the competition between HMFOR and OER at high potentials [30,31]. The maximum current density over the whole scanning window is 17.5 mA cm^{-2} , which is much lower than the value of potentiodynamic LSV curve (41.1 mA cm^{-2} at the scan rate of 5 mV s^{-1}).

To investigate the correlation between electrolytic efficiency and the properties of catalysts, $\text{Ni}(\text{OH})_2/\text{CC}$ electrodes doped with different element (Fe, Co, Mo, Mn, Cr, Ga) were prepared by a facile one-step hydrothermal reaction. The X-ray diffraction (XRD) patterns of the

prepared samples reveal that most of the diffraction peaks match well with the rhombohedral $\text{Ni}(\text{OH})_2$ (JCPDS 38-0715) (Fig. 1c), the diffraction peak at 19.2° is assigned to the hexagonal $\text{Ni}(\text{OH})_2$ (JCPDS 14-0117), indicating that the six elements are doped into the lattice of $\text{Ni}(\text{OH})_2$ and no corresponding oxides/hydroxides of the doped elements are formed. After CV cycles, the XRD patterns show only rhombohedral $\text{Ni}(\text{OH})_2$ was retained (Fig. S2). The characteristic peak of hexagonal $\text{Ni}(\text{OH})_2$ disappears almost completely, implying conversion to an amorphous form during the reaction. Furthermore, SEM images clearly shows all electrode surfaces are typical 2D nanosheet structures (Fig. S3), the walls of carbon clothes are completely covered by a compact arrangement of vertically growing $\text{Ni}(\text{OH})_2$. In addition, the EDS mapping images in Fig. S4 indicate that Ni, O and doped elements are uniformly dispersed over the entire carbon cloth. Quantitative elemental analysis shows that the content of doping elements (Co, Mn, Fe, Cr, Mo, Ga) varies between 4% and 9% (Table S1). Besides, the well-defined morphology of 2D nanosheets can also be seen in the TEM images (Fig. S5) whereas the lattice spacing corresponds to the typical crystalline phase of $\text{Ni}(\text{OH})_2$, the subtle difference in crystalline spacing is due to the different types and contents of doping atoms.

The HMF electrooxidation properties of X- $\text{Ni}(\text{OH})_2$ were examined using LSV scans (Fig. 1d) and five-point segmented chronoamperometry (Fig. 1e and S6). Among the LSV curves, Co- $\text{Ni}(\text{OH})_2$ has the lowest onset potential at the same scan rate, which is consistent with previous reports [2]. However, the anodic peak current density of Co- $\text{Ni}(\text{OH})_2$ within the voltage window obtained by segmented i-t is only 25.7 mA cm^{-2} , which is the lowest of all samples. Cr- $\text{Ni}(\text{OH})_2$ has a higher onset potential but can reach the highest current density of 75 mA cm^{-2} , indicating that a low onset overpotential does not mean a high current density for HMF electrooxidation can be achieved. For reasons of electrolytic efficiency, the anodic peak current density that can be achieved within the voltage window is actually a better indicator of catalyst performance than onset overpotential. Of note, as exhibited by LSV curves (Fig. 1d), the maximum current density of Fe- $\text{Ni}(\text{OH})_2$ is 37.8 mA cm^{-2} , the lowest among all samples. However, obtained by

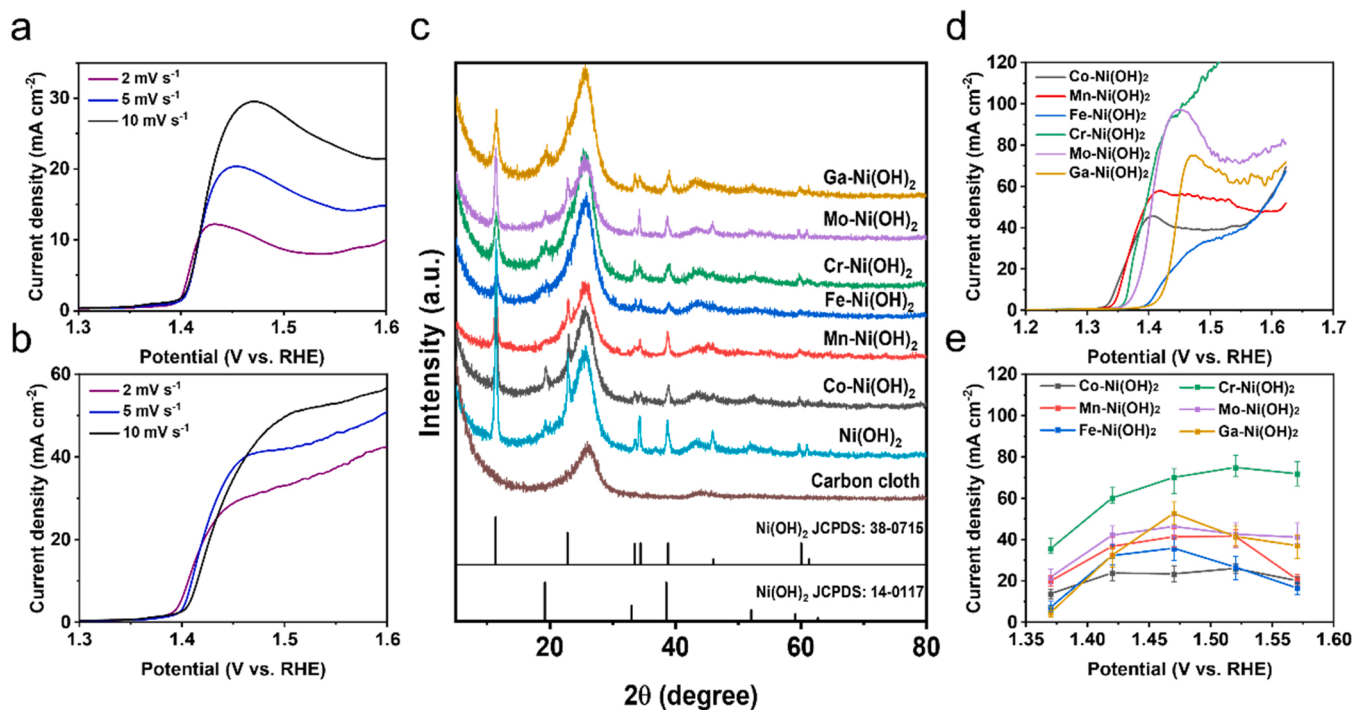


Fig. 1. (a-b) LSV curves of $\text{Ni}(\text{OH})_2/\text{CC}$ in 1 M KOH with (a) and without (b) 10 mM HMF at different scan rates. (c) XRD patterns of the $\text{Ni}(\text{OH})_2/\text{CC}$ doped with different metal elements. (d) LSV curves of X- $\text{Ni}(\text{OH})_2/\text{CC}$ in 1 M KOH with 10 mM HMF. (e) The actual current density of X- $\text{Ni}(\text{OH})_2/\text{CC}$ obtained by segmented chronoamperometry for HMFOR.

segmented *i*-*t* (Fig. 1e), the maximum actual current density of Fe-Ni(OH)₂ is 35.9 mA cm⁻², higher than that of Co-Ni(OH)₂ (26.5 mA cm⁻²), and the same is true for Ga-Ni(OH)₂ vs. Mo-Ni(OH)₂, further illustrating the limitations of the LSV curves in comparing catalytic performance.

Given the high sensitivity of Fourier-transformed alternating current voltammetry (FTACV) to electron transfer and devoid of non-faradaic background current contributions, use of large amplitude Fourier transformed ac voltammetry and comprehensive analysis of the higher harmonics has enabled us to access the redox processes responsible for catalysis [32,33]. we attempted to apply FTACV in HMFOR process (Fig. 2a). The strong response signal in the 4th harmonic component corresponds to the charge transfer during Ni²⁺ oxidation. It can be seen that Co-Ni(OH)₂ has a very obvious response signal at 1.3 V, indicating that it is more favorable for the oxidation of Ni²⁺, while Fe-Ni(OH)₂ and Ga-Ni(OH)₂ do not show a response signal until 1.39 V, which is corresponding to onset overpotential in the performance tests (Fig. 1d). The electrochemical surface areas (ECSA) were compared by calculating their electrochemical double-layer capacitance (*C*_{dl}). As shown in Figs. S7 and 2b, the *C*_{dl} values of X-Ni(OH)₂ are very close to each other, while the maximum currents normalized by the electrochemically active surface area show significant differences (Fig. 2c), so that the differences in the anodic peak currents can be excluded as a result of the electrochemical surface area. The turnover frequency (TOF) for HMFOR is also used to exhibit the difference in intrinsic activity (Fig. 2d), Fe-Ni(OH)₂ has the fastest intrinsic conversion frequency, but the presence of Fe in Fe-Ni(OH)₂ significantly inhibits the oxidation of Ni²⁺ [34,35], resulting in fewer available active sites on the Fe-Ni(OH)₂ surface and thus limiting the activity of Fe-Ni(OH)₂. The TOF value of Cr-Ni(OH)₂ is second only to Fe-Ni(OH)₂ and much higher than other comparison samples, suggesting the prominent intrinsic HMFOR activity.

Electrolysis experiments were carried out for the oxidation of HMF using X-Ni(OH)₂/CC as electrodes in H-type cell at the potential of 1.47 V. The changes in the concentration of HMF, intermediates and oxidation products were quantified by HPLC. The oxidation of one HMF molecule to FDCA requires six electrons, so the complete conversion of

2×10^{-4} mol HMF (10 mM HMF in 20 mL electrolyte) requires a theoretical charge of 115.8 C. Fig. S8 clearly demonstrate the gradual decrease of HMF concentration with the increase of electrolysis time, accompanied by the gradual increase of FDCA concentration and the generation of a small amount of intermediate products HMFCa and FFCA. When the passed charge reached 116 C, HMF almost completely disappeared and the conversion rate was close to 100%. In the comparison of six X-Ni(OH)₂/CC samples, Cr-Ni(OH)₂/CC requires the shortest electrolysis time of 1.6 h, while Co-Ni(OH)₂/CC requires 4.56 h (Fig. S9). In addition, the selectivity of FDCA on Cr-Ni(OH)₂/CC can reach over 95.5% with a Faradic efficiency of 96% (Fig. 2e). In contrast, only 82.1% selectivity with 82.7% FE can be obtained with Co-Ni(OH)₂/CC. This is probably due to the fact that HMF is not stable under alkaline conditions and is prone to dimerization reactions [5,36,37]. The longer the electrolysis time, the more HMF is consumed by the polymerization reaction, which leads to a decrease in selectivity and Faradic efficiency. This experiment further demonstrates the importance of high current electrolysis for efficient and selective FDCA production.

3.2. The correlation between maximum current and the reduction of Ni³⁺

Investigation of the relationship between the anodic peak current and the properties of the electrode materials is essential for both the refinement of the theory and the design of highly efficient catalysts. The in-situ Raman spectra are collected at various applied potentials to observe the dynamic transformation between Ni(OH)₂ and NiOOH under OER and HMFOR (Fig. 3a-b). As can be read, the Ni(OH)₂/CC electrode exhibits two peaks under potentials below 1.4 V, which are assigned to Ni²⁺-O. For OER process, the Ni(OH)₂ dehydrogenates to form NiOOH and further accumulation after 1.35 V, which can be identified by the peaks at 475 and 555 cm⁻¹ [38,39], at higher potentials, especially after the occurrence of OER, the generation of surface gas film affect the focusing clarity of the Raman lens, thus leading to the weakening of peak intensity. After adding HMF, the signals of Ni³⁺-O vibrations were not recorded until 1.45 V. It is notable that the dynamic transformation from Ni²⁺ to Ni³⁺ does exist during HMFOR below

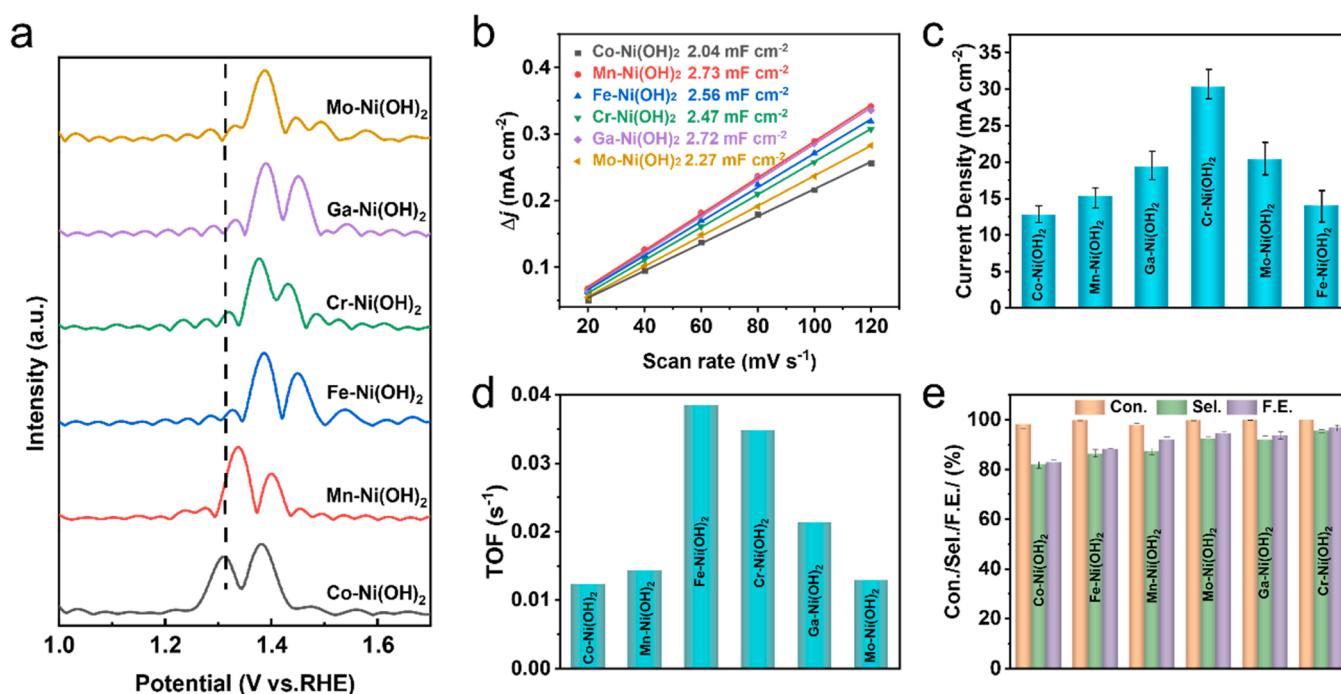


Fig. 2. (a) 4th harmonic components of ac voltammograms ($f = 9.02$ Hz, $\Delta E = 0.08$ V) for HMFOR. (b) The variation of current densities plotted against the scan rate at 1.02 V vs. RHE for X-Ni(OH)₂/CC. (c) The anodic peak current densities normalized by ECSA. (d) Calculated TOFs of X-Ni(OH)₂ for HMFOR. (e) HMF conversion, FDCA selectivity and FE of different X-Ni(OH)₂/CC.

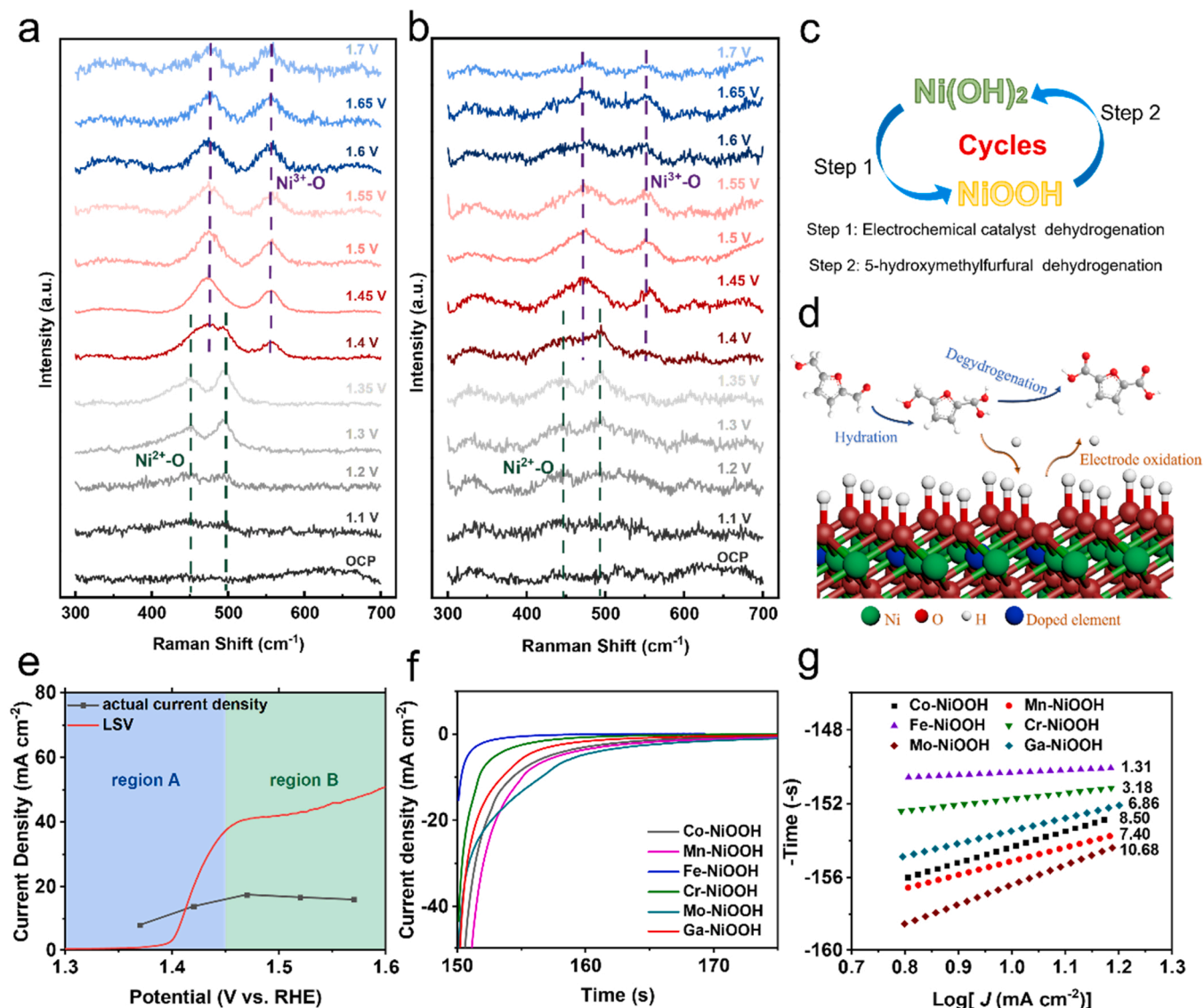


Fig. 3. *In-situ* Raman spectra of Ni(OH)₂/CC under various potentials in 1.0 M KOH electrolyte without (a) and with (b) HMF (b). (c) HMFOR mechanism including electrocatalysts oxidation and non-electrochemical step. (d) Schematic diagram of PCET process on the surface of Ni(OH)₂. (e) LSV curve and actual current densities of HMFOR when Ni(OH)₂ is used as working electrode. (f) Reduction curves of X-NiOOH with HMF added after pre-oxidation. (g) Corresponding slopes of reduction.

1.45 V, the NiOOH formed at low voltages is rapidly reduced by the reaction with HMF such that no accumulation. The HMFOR consists of two steps, the electro-oxidation process of Ni²⁺ combined with the PCET process of HMF dehydrogenation to form a cyclic reaction (Fig. 3c-d). According to our tests and previous reports, the magnitude of the onset potential is closely related to the Ni²⁺ oxidation. XPS spectra reveals the state of Ni²⁺ and doped elements in different X-Ni(OH)₂ (Figs. S10 and S11). Compared with Ni(OH)₂, the positions of Ni²⁺ peaks in different elements doping have obvious shifts, among which the position of Ni²⁺ peaks in Co-Ni(OH)₂ has the largest shift toward high binding energy, indicating that Ni²⁺ is in a more oxidizable state, while Ni²⁺ in Fe-Ni(OH)₂ is in the least oxidizable state [19,40]. This is consistent with the onset potential of Ni²⁺ oxidation in the LSV curves without HMF (Fig. S12). The lowest onset potential (1.32 V) of the oxidation peak of Co-Ni(OH)₂ corresponds to the highest binding energy of Ni 2p in the XPS spectrum, while the highest onset potentials (1.39 V) of Ga-Ni(OH)₂ and Fe-Ni(OH)₂ have the lowest binding energy of Ni 2p. However, according to the above discussion, the onset overpotential does not explain the difference in anodic peak current. Combined with the results of *in-situ* Raman, we believe that the process of HMFOR with in the

voltage window can be divided into two regions (Fig. 3e). In region A (voltage below 1.50 V), the potential is the key factor affecting the reaction rate and the formed Ni³⁺ is consumed rapidly, the current density of HMFOR gradually increases with increasing voltage; in region B, there is an accumulation of Ni³⁺ and the current density of HMFOR tends to be constant and subsequently competes with OER, the rate-determining step is the reduction of NiOOH. To verify this assumption, we explored the PCET step of Ni³⁺ reduction-coupled HMF dehydrogenation between different X-Ni(OH)₂. The CV curves of different X-Ni(OH)₂ in 1.0 M KOH are shown in Fig. S13. During one CV cycle, part of Ni²⁺ is difficult to reduce after oxidation and maintains the NiOOH state, so the ratio of charge of the reduction peak to the oxidation peak can be considered as the percentage of Ni³⁺ that can be rapidly reduced in all available Ni sites and used to compare the strength of reducibility. It is found that Fe-Ni(OH)₂ has the highest ratio, followed by Cr-Ni(OH)₂, and there is a significant positive correlation between the order of the ratios and the calculated TOF values (Fig. S14), which indicates that the reducibility of Ni³⁺ is an important factor affecting the intrinsic activity. Besides, the reduction curves can also be measured by segmented i-t, first, the potential of 1.47 V was set for 150 s to enrich the

X-NiOOH intermediate, then the potential was switched to open circuit potential and injected HMF to monitor the transient current change (Figs. 3f and S15). According to the calculation of Tafel slope, the reduced slope can be obtained (Fig. 3g), the slope of Fe-Ni(OH)₂ is 1.31 s dec⁻¹, obviously smaller than those X-Ni(OH)₂, indicating the faster catalytic HMFOR kinetics, which is consistent with the calculation of TOF.

Subsequently, in-situ Raman spectra were further used to record the dynamic changes of Ni³⁺ during reduction (Fig. S16). First, Ni(OH)₂ was oxidized to NiOOH by using Ni as the working electrode in 1.0 M KOH without HMF at the potential of 1.5 V for 180 s. Subsequently, HMF was added to react with NiOOH and monitored the changes of the characteristic peaks of Ni³⁺-O on the catalyst surface. Fig. S16 shows the appearance of the characteristic peaks of Ni³⁺-O and the accumulation of NiOOH on the surface of all six groups of samples in the initial state, after addition of HMF, the peaks of Ni³⁺-O weaken and eventually disappear. In contrast, Mo-Ni(OH)₂ still has a small amount of Ni³⁺-O residue until after 12 s, while Ni³⁺-O accumulated in Cr-Ni(OH)₂ disappeared almost completely after 3 s, demonstrating its faster reduction rate. Due to the higher oxidation energy barrier, Fe-Ni(OH)₂ still has a large amount of Ni²⁺ coexisting with Ni³⁺-O under the potential of 1.5 V, and the vibrational peak of Ni³⁺-O is also rapidly annihilated at a faster reduction rate. Operando electrochemical impedance spectroscopy (EIS) was also performed to further investigate the interface behavior and catalytic kinetics of X-Ni(OH)₂. The corresponding bode plots for OER and HMFOR show two electrochemical processes (Figs. S17 and S18), the high frequency region (10¹-10⁵ Hz) is corresponding to the oxidation of electrode inner and the low frequency region is associated with interface reaction charge, namely the appearance of oxidation species at the electrode interface [41–43]. Compared with OER, The peaks appearing in the low frequency region during HMFOR

are significantly reduced, indicating the oxidized surface is partially reduced by HMF. Furthermore, the peaks in low frequency region at the potential of 1.42–1.52 V_{RHE} for Fe-Ni(OH)₂ and Cr-Ni(OH)₂ are shifted to the higher frequency, implying accelerated interfacial charge transfer, that is accelerated reduction of Ni³⁺ and oxidation of HMF.

3.3. DFT calculations

To theoretically understand the effect of the PCET process on the anodic peak current, density functional theory (DFT) calculations were carried out to reveal the hydrogen transfer energy barrier. The essence of HMF electrooxidation is the transfer of hydrogen protons from the substrate molecule to NiOOH. Under alkaline conditions, the aldehyde group in the HMF molecule is first hydrated to a diol group, then dehydrogenation of alpha-C-H and hydroxyl take place one by one to form carboxyl group. After that, the alpha-C-H and hydroxyl groups on the hydroxyl side are dehydrogenated in turn to form aldehyde, followed by hydration and dehydrogenation steps, leading to the formation of FDCA [16]. In the case of NiOOH doped with different elements, we first checked the most stable doping sites and optimized the adsorption state of HMF on its surface. The energy barriers of hydrogen proton transfer from HMF to NiOOH surface were calculated on the optimized model (Fig. 4a). As shown in Fig. 4b-c, the calculated kinetic barrier of hydrogen transfer from HMF molecule to Fe doped NiOOH surface was 0.7626 (eV), with a reaction free energy (ΔG_H) of -0.5313 eV, demonstrating the spontaneity of the PCET process. In contrast, the hydrogen transfer energy barrier on the surface of Mo-NiOOH is 1.221 eV, as indicated by the most positive ΔG_H of 0.0882 eV, manifesting the difficulty of hydrogen transfer from HMF molecule to Mo-NiOOH. Besides, on the external surface of Cr, Ga, Mn and Co doped NiOOH, the hydrogen transfer barriers were calculated to be 0.9238 eV,

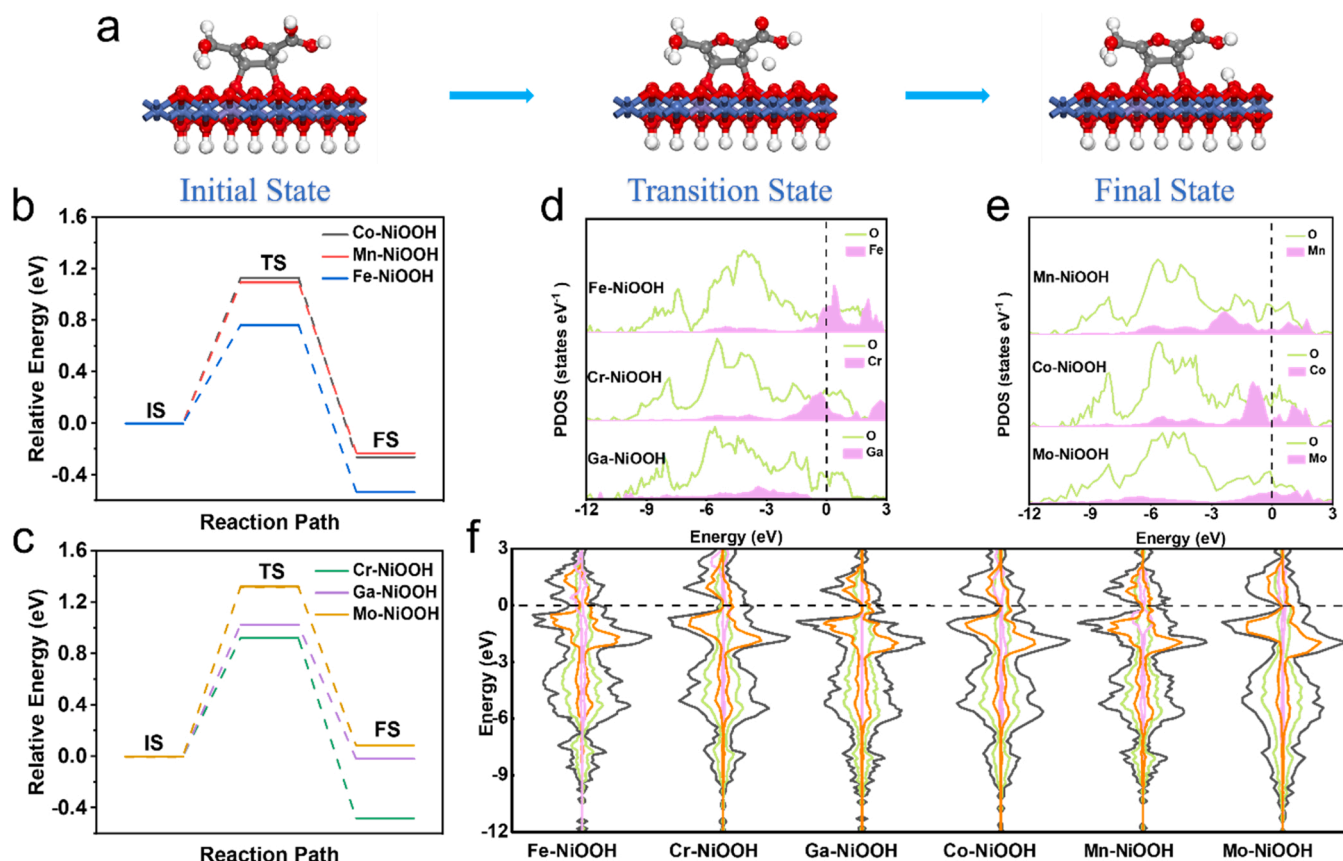


Fig. 4. (a) The optimized model and the initial, transition and final states in the hydrogen transfer process. (b-c) Energy changes in the hydrogen transfer process on different X-NiOOH surfaces. (d-e) Comparison of PDOS of doped elements and O. (f) DOS plots of X-NiOOH. The fermi level are highlighted.

1.0264 eV, 1.092 eV and 1.1286 eV, respectively. The lower the hydrogen transfer energy barrier, the faster the rate of the PCET process, the faster the cycle between the oxidation of Ni^{2+} and the dehydrogenation of HMF, and the higher the anodic peak current. To comprehend the differences in hydrogen transfer energy barriers on the surface of NiOOH doped with different metal elements, the charge density was calculated to investigate the charge distribution. As displayed in Fig. 4d-e, compared with other metal elements, there are evident overlapping regions among Fe 3d and O 2p, Cr 3d and O 2p bands, indicating the stronger covalent hybridization between oxygen ligands and Fe/Cr sites [44,45]. More importantly, Fe-NiOOH and Cr-NiOOH have a higher charge density near the Fermi energy level and are stronger nucleophilic, and more likely to capture hydrogen protons from HMF molecules (Fig. 4f). [4,46].

3.4. Maximizing the performance of $\text{Ni}(\text{OH})_2$ by doping Cr

According to the above discussion, the PCET process of Ni^{3+} reduction to Ni^{2+} coupled with HMF dehydrogenation is the key to moderate the anodic peak current density. Therefore, to achieve high current density HMF oxidation, the accumulation of Ni sites is required on the one hand, and the rate of Ni^{3+} reduction during the reaction needs to be accelerated to enhance the intrinsic activity of individual Ni sites on the

other. Doping of heteroelements in the $\text{Ni}(\text{OH})_2$ lattice can effectively change the local charge distribution around Ni sites, therefore changing the reduction rate of Ni^{3+} . Theoretical and experimental evidence shows that the introduction of Fe in the lattice can significantly accelerate the proton transfer rate during the reduction of NiOOH, which results in the highest intrinsic activity of HMFOR. However, the presence of Fe inhibits the oxidation of Ni^{2+} , rendering the availability of Ni sites in Fe-Ni $(\text{OH})_2$ limited and therefore unsuitable for the development of efficient catalysts. In contrast, Cr doping can also markedly decrease the hydrogen transfer energy barrier and accelerate the dehydrogenation process of HMF, and the utilization rate of the Ni^{2+} site is much higher than Fe doping, making it the best choice for the development of high current density for HMFOR. So Cr-Ni $(\text{OH})_2$ nanosheets with different Cr doping ratios supported on Ni foam were synthesized by a facile hydrothermal reaction. XRD patterns demonstrate that the diffraction peaks of three samples match well with $\text{Ni}(\text{OH})_2$ (JCPDS 38-0715) along with the NF substrate (Fig. S19). SEM images of three samples showing Ni foam surfaces wrapped by densely arranged arrays Cr-Ni $(\text{OH})_2$ nanosheets (Fig. 5a-c). The ratios of Cr doping, given by EDS, are 1.07%, 1.42%, and 2.11% (Fig. S20). These values coincide with the increase of $\text{Cr}(\text{NO}_3)_3 \cdot 6\text{H}_2\text{O}$ added in the hydrothermal reaction. The performance of three samples for HMF oxidation was observed by segmented chronoamperometry. As shown in Fig. 5d, Cr-Ni $(\text{OH})_2$ /NF with Cr doping of

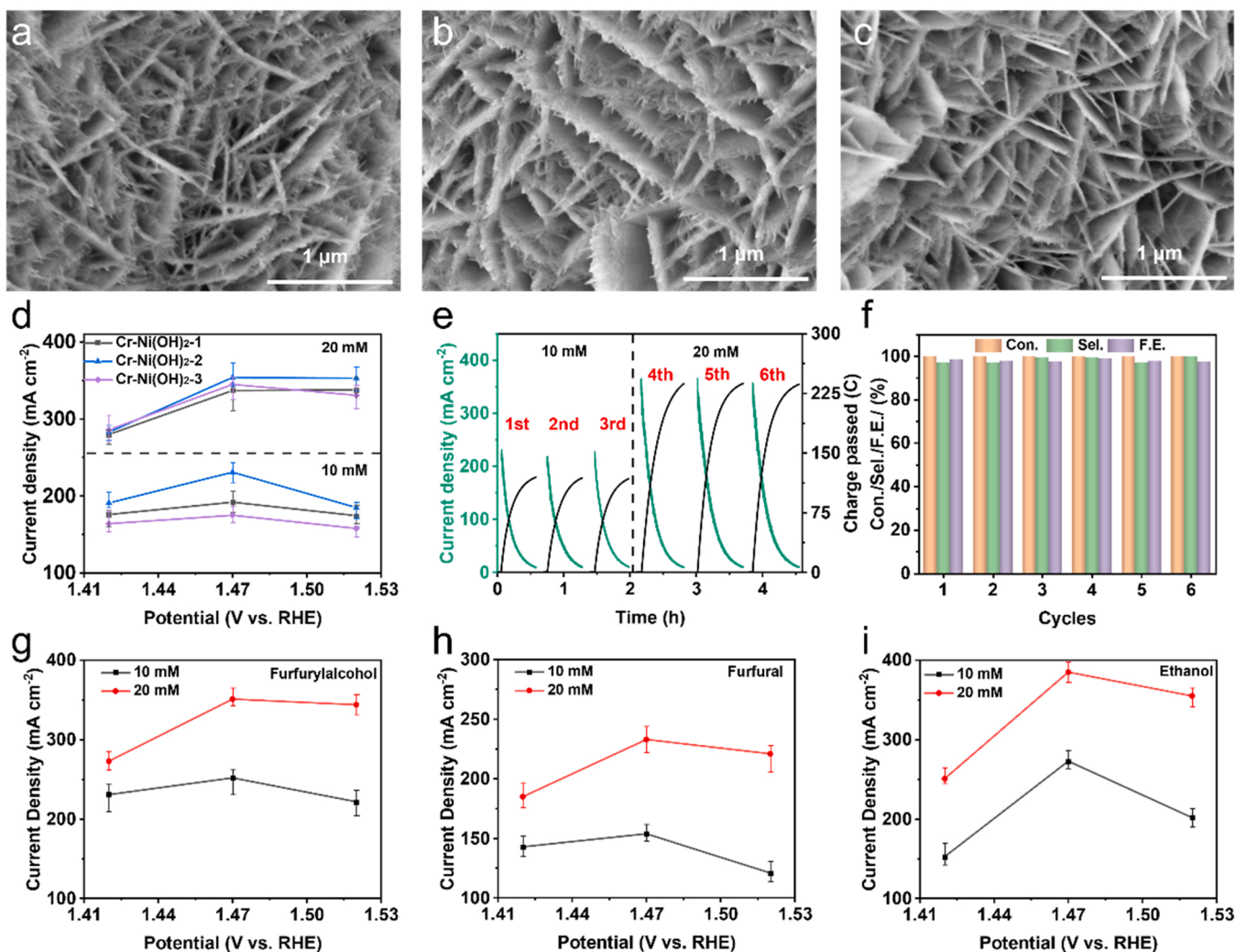


Fig. 5. (a-c) SEM images of as-synthesized Cr-Ni(OH)₂/NF with different Cr doping amounts. (d) Current densities of Cr-Ni(OH)₂/NF at HMF concentrations of 10 and 20 mM. (e) Current densities and charge-time during the electrooxidation of HMF of Cr-Ni(OH)₂/NF-2. (f) HMF conversion, selectivity of FDCA and FE obtained by the Cr-Ni(OH)₂/NF for six consecutive cycles of HMFOR. (g-i) The electrocatalytic performance of Cr-Ni(OH)₂/NF for furfuralcohol, furfural and ethanol oxidation.

1.42% can achieve the current density of 230 mA cm^{-2} at HMF concentration of 10 mM, much higher than at Cr doping of 1.07% and 2.11%. When the HMF concentration increases to 20 mM, the current density can reach more than 360 mA cm^{-2} , showing extremely high activity of HMF oxidation.

The chronoamperometric electrolysis measurement of Cr-Ni(OH)₂/NF-2 were also performed at the potential of 1.47 V to quantify efficiency, conversion and selectivity. When the concentration of HMF is 10 mM (20 mL electrolyte), the electron transfer number could reach 116 C in only 32 min, the measured conversion of HMF is close to 100%, and the selectivity is as high as 98% (Fig. S21). Even if the concentration of HMF increases to 20 mM, the Cr-Ni(OH)₂/NF-2 electrode also can complete convert HMF within 40 min and maintain a high selectivity, which further demonstrate that excellent reaction kinetics can be obtained on Cr-Ni(OH)₂/NF electrode. Such efficient transformation ranks among the top in the literatures for HMFOR reported until now (Table S2).

The stability of Cr-Ni(OH)₂/NF electrode was measured by cycling three times the electrolysis at 10 mM of HMF and then three times at 20 mM (Fig. 5e). During the six electrolysis processes, the initial current density did not decrease significantly, and the conversion of HMF was close to 100% when the transfer charge number reached 116/232 C, and the selectivity of FDCA also remained above 98% (Fig. 5f). SEM images indicate no evident change in the morphology of the nanosheet arrays on the NF surface after stability testing (Fig. S22), and EDS shows that the content of Cr is 1.38% at the end of HMFOR (Fig. S23), which is not significantly different from that before the reaction (1.42%). This confirms the excellent stability of Cr-Ni(OH)₂/NF electrode for HMF electrooxidation. Finally, we tested the electrocatalytic performance of Cr-Ni(OH)₂/NF-2 on furfuryl alcohol, furfural and ethanol (Fig. 5g-i, S24). The results showed that the electrode designed based on the modulated Ni³⁺ reduction could achieve efficient conversion of the three alcohol-formaldehyde substrates, and the current could reach over 150 mA cm^{-2} at a substrate concentration of 10 mM. This test demonstrates the versatility of Cr-Ni(OH)₂/NF for electrocatalysis of biomass molecules.

4. Conclusions

First, we demonstrate the limitations of LSV curves in evaluating the Ni-based catalysts for HMF electrooxidation activity. The current density exhibited by the LSV curve is falsely high due to the presence of Ni²⁺ oxidation peaks in the HMF electrooxidation potential interval. In order to accurately assess the activity, we propose to use segmented i-t to show the actual current density of Ni-based electrodes for HMFOR. For the sake of electrolysis efficiency, we chose to use the anodic peak current density rather than the overpotential to compare the activity of the electrodes. By measuring the activity and dynamic Ni(OH)₂-NiOOH transformation of nickel hydroxide doped with six different elements, we found that the maximum current density is closely related to the PCET process of Ni³⁺ reduction. Theoretical calculations showed that the PCET process on the surface of Fe/Cr-doped NiOOH has lower hydrogen transfer energy barriers, stronger covalent hybridization between metal sites and oxygen ligands with higher charge density makes it easier to capture hydrogen protons from HMF molecules. Finally, we obtained the electrode that can achieve high efficiency conversion of HMF by optimizing Cr-doped Ni(OH)₂/NF. This electrode can achieve complete conversion of $2 \times 10^{-4} \text{ mol HMF}$ within 32 min, with a selectivity of over 98% for FDCA. This work demonstrates a long-standing misconception about catalyst performance evaluation and lays the foundation for the design of catalysts that are truly capable of high current density.

CRedit authorship contribution statement

Zhaohui Yang: Methodology, Investigation, Data curation, Writing

– original draft. **Baolong Zhang:** Methodology, Investigation, Data curation, Writing – original draft. **ChuanYu Yan:** Methodology, Writing – review & editing. **Zhimin Xue:** Conceptualization, Methodology, Supervision. **Tiancheng Mu:** Conceptualization, Writing – review & editing, Supervision.

Declaration of Competing Interest

The authors declare that they have no known competing financial interests or personal relationships that could have appeared to influence the work reported in this paper.

Data availability

Data will be made available on request.

Acknowledgements

The authors thank the National Natural Science Foundation of China (22073112) for financial support.

Appendix A. Supporting information

Supplementary data associated with this article can be found in the online version at doi:10.1016/j.apcatb.2023.122590.

References

- [1] M.T. Bender, X. Yuan, K.-S. Choi, Alcohol oxidation as alternative anode reactions paired with (photo)electrochemical fuel production reactions, *Nat. Commun.* 11 (2020) 4594.
- [2] W. Chen, C. Xie, Y. Wang, Y. Zou, C.-L. Dong, Y.-C. Huang, Z. Xiao, Z. Wei, S. Du, C. Chen, B. Zhou, J. Ma, S. Wang, Activity origins and design principles of nickel-based catalysts for nucleophile electrooxidation, *Chem* 6 (2020) 2974–2993.
- [3] B. You, X. Liu, N. Jiang, Y. Sun, A general strategy for decoupled hydrogen production from water splitting by integrating oxidative biomass valorization, *J. Am. Chem. Soc.* 138 (2016) 13639–13646.
- [4] Z. He, J. Hwang, Z. Gong, M. Zhou, N. Zhang, X. Kang, J.W. Han, Y. Chen, Promoting biomass electrooxidation via modulating proton and oxygen anion deintercalation in hydroxide, *Nat. Commun.* 13 (2022) 3777.
- [5] R. Ge, Y. Wang, Z. Li, M. Xu, S.M. Xu, H. Zhou, K. Ji, F. Chen, J. Zhou, H. Duan, Selective electrooxidation of biomass-derived alcohols to aldehydes in a neutral medium: promoted water dissociation over a nickel-oxide-supported ruthenium single-atom catalyst, *Angew. Chem. Int. Ed.* 61 (2022), e202200211.
- [6] L. Jiang, A. Gonzalez-Diaz, J. Ling-Chin, A. Malik, A.P. Roskilly, A.J. Smallbone, PEF plastic synthesized from industrial carbon dioxide and biowaste, *Nat. Sustain.* 3 (2020) 761–767.
- [7] J. Woo, B.C. Moon, U. Lee, H.-S. Oh, K.H. Chae, Y. Jun, B.K. Min, D.K. Lee, Collaborative Electrochemical Oxidation of the Alcohol and Aldehyde Groups of 5-Hydroxymethylfurfural by NiOOH and Cu(OH)₂ for Superior 2,5-Furandicarboxylic Acid Production, *ACS Catal.* 12 (2022) 4078–4091.
- [8] C. Xu, E. Paone, D. Rodríguez-Padrón, R. Luque, F. Mauriello, Recent catalytic routes for the preparation and the upgrading of biomass derived furfural and 5-hydroxymethylfurfural, *Chem. Soc. Rev.* 49 (2020) 4273–4306.
- [9] C. Tang, Y. Zheng, M. Jaroniec, S.-Z. Qiao, Electrocatalytic refinery for sustainable production of fuels and chemicals, *Angew. Chem. Int. Ed.* 60 (2021) 19572–19590.
- [10] B. You, N. Jiang, X. Liu, Y. Sun, Simultaneous H₂ generation and biomass upgrading in water by an efficient noble-metal-free bifunctional electrocatalyst, *Angew. Chem. Int. Ed.* 55 (2016) 9913–9917.
- [11] P. Zhou, X. Lv, S. Tao, J. Wu, H. Wang, X. Wei, T. Wang, B. Zhou, Y. Lu, T. Frauenheim, X. Fu, S. Wang, Y. Zou, Heterogeneous-interface-enhanced adsorption of organic and hydroxyl for biomass electrooxidation, *Adv. Mater.* 34 (2022), 2204089.
- [12] J. Weidner, S. Barwe, K. Sliozberg, S. Piontek, J. Masa, U.-P. Apfel, W. Schuhmann, Cobalt-metalloid alloys for electrochemical oxidation of 5-hydroxymethylfurfural as an alternative anode reaction in lieu of oxygen evolution during water splitting, *Beilstein. J. Org. Chem.* 14 (2018) 1436–1445.
- [13] X. Deng, G.Y. Xu, Y.J. Zhang, L. Wang, J. Zhang, J.F. Li, X.Z. Fu, J.L. Luo, Understanding the Roles of Electrogenated Co(3+) and Co(4+) in Selectivity-Tuned 5-Hydroxymethylfurfural Oxidation, *Angew. Chem. Int. Ed.* 60 (2021) 20535–20542.
- [14] L. Gao, Z. Liu, J. Ma, L. Zhong, Z. Song, J. Xu, S. Gan, D. Han, L. Niu, NiSe@NiOx core-shell nanowires as a non-precious electrocatalyst for upgrading 5-hydroxymethylfurfural into 2,5-furandicarboxylic acid, *Appl. Catal. B Environ.* 261 (2020), 118235.

- [15] G. Yang, Y. Jiao, H. Yan, Y. Xie, A. Wu, X. Dong, D. Guo, C. Tian, H. Fu, Interfacial engineering of MoO₂-FeP heterojunction for highly efficient hydrogen evolution coupled with biomass electrooxidation, *Adv. Mater.* 32 (2020), 2000455.
- [16] W. Chen, Y. Wang, B. Wu, J. Shi, Y. Li, L. Xu, C. Xie, W. Zhou, Y.C. Huang, T. Wang, S. Du, M. Song, D. Wang, C. Chen, J. Zheng, J. Liu, C.L. Dong, Y. Zou, J. Chen, S. Wang, Activated Ni-OH bonds in a catalyst facilitates the nucleophile oxidation reaction, *Adv. Mater.* 34 (2022), e2105320.
- [17] S. Barwe, J. Weidner, S. Cychy, D.M. Morales, S. Dieckhöfer, D. Hiltrop, J. Masa, M. Muhler, W. Schuhmann, Electrocatalytic oxidation of 5-(hydroxymethyl) furfural using high-surface-area nickel boride, *Angew. Chem. Int. Ed.* 57 (2018) 11460–11464.
- [18] Y. Xie, Z. Zhou, N. Yang, G. Zhao, An overall reaction integrated with highly selective oxidation of 5-hydroxymethylfurfural and efficient hydrogen evolution, *Adv. Funct. Mater.* 31 (2021), 202102886.
- [19] X. Lu, K.H. Wu, B. Zhang, J. Chen, F. Li, B.J. Su, P. Yan, J.M. Chen, W. Qi, Highly Efficient Electro-reforming of 5-Hydroxymethylfurfural on Vertically Oriented Nickel Nanosheet/Carbon Hybrid Catalysts: Structure-Function Relationships, *Angew. Chem. Int. Ed.* 60 (2021) 14528–14535.
- [20] Y. Yang, D. Xu, B. Zhang, Z. Xue, T. Mu, Substrate molecule adsorption energy: An activity descriptor for electrochemical oxidation of 5-Hydroxymethylfurfural (HMF), *Chem. Eng. J.* 433 (2022).
- [21] Y. Lu, T. Liu, Y.-C. Huang, L. Zhou, Y. Li, W. Chen, L. Yang, B. Zhou, Y. Wu, Z. Kong, Z. Huang, Y. Li, C.-L. Dong, S. Wang, Y. Zou, Integrated Catalytic Sites for Highly Efficient Electrochemical Oxidation of the Aldehyde and Hydroxyl Groups in 5-Hydroxymethylfurfural, *ACS Catal.* 12 (2022) 4242–4251.
- [22] Z. Zhou, Y.-n Xie, L. Sun, Z. Wang, W. Wang, L. Jiang, X. Tao, L. Li, X.-H. Li, G. Zhao, Strain-induced in situ formation of NiOOH species on CoCo bond for selective electrooxidation of 5-hydroxymethylfurfural and efficient hydrogen production, *Appl. Catal. B Environ.* 305 (2022), 121072.
- [23] N. Zhang, Y. Zou, L. Tao, W. Chen, L. Zhou, Z. Liu, B. Zhou, G. Huang, H. Lin, S. Wang, Electrochemical oxidation of 5-hydroxymethylfurfural on nickel nitride/carbon nanosheets: reaction pathway determined by in situ sum frequency generation vibrational spectroscopy, *Angew. Chem. Int. Ed.* 58 (2019) 15895–15903.
- [24] J.N. Hausmann, P.V. Menezes, G. Vijaykumar, K. Laun, T. Diemant, I. Zebger, T. Jacob, M. Driess, P.W. Menezes, In-Liquid Plasma Modified Nickel Foam: NiOOH/NiFeOOH Active Site Multiplication for Electrocatalytic Alcohol, Aldehyde, and Water Oxidation, *Adv. Energy Mater.* 12 (2022), 2202098.
- [25] I. Mondal, J.N. Hausmann, G. Vijaykumar, S. Mebs, H. Dau, M. Driess, P. W. Menezes, Nanostructured Intermetallic Nickel Silicide (Pre)Catalyst for Anodic Oxygen Evolution Reaction and Selective Dehydrogenation of Primary Amines, *Adv. Energy Mater.* 12 (2022), 2200269.
- [26] B. Zhang, H. Fu, T. Mu, Hierarchical NiSx/Ni₂P nanotube arrays with abundant interfaces for efficient electrocatalytic oxidation of 5-hydroxymethylfurfural, *Green. Chem.* 24 (2022) 877–884.
- [27] S. Yang, Y. Guo, Y. Zhao, L. Zhang, H. Shen, J. Wang, J. Li, C. Wu, W. Wang, Y. Cao, S. Zhuo, Q. Zhang, H. Zhang, Construction of Synergistic Ni₃S₂-MoS₂ Nanoheterojunctions on Ni Foam as Bifunctional Electrocatalyst for Hydrogen Evolution Integrated with Biomass Valorization, *Small* 18 (2022), 2201306.
- [28] Y. Sun, J. Wang, Y. Qi, W. Li, C. Wang, Efficient Electrooxidation of 5-Hydroxymethylfurfural Using Co-Doped Ni₃S₂ Catalyst: Promising for H₂ Production under Industrial-Level Current Density, *Adv. Sci.* 9 (2022), e2200957.
- [29] B. Zhou, C.-L. Dong, Y.-C. Huang, N. Zhang, Y. Wu, Y. Lu, X. Yue, Z. Xiao, Y. Zou, S. Wang, Activity origin and alkalinity effect of electrocatalytic biomass oxidation on nickel nitride, *J. Energy Chem.* 61 (2021) 179–185.
- [30] Y. Song, Z. Li, K. Fan, Z. Ren, W. Xie, Y. Yang, M. Shao, M. Wei, Ultrathin layered double hydroxides nanosheets array towards efficient electrooxidation of 5-hydroxymethylfurfural coupled with hydrogen generation, *Appl. Catal. B Environ.* 299 (2021), 120669.
- [31] M. Park, M. Gu, B.-S. Kim, Tailorable electrocatalytic 5-hydroxymethylfurfural oxidation and H₂ production: architecture–performance relationship in bifunctional multilayer electrodes, *ACS Nano* 14 (2020) 6812–6822.
- [32] Y. Zhang, X. Zhang, Y. Ling, F. Li, A.M. Bond, J. Zhang, Controllable Synthesis of Few-Layer Bismuth Subcarbonate by Electrochemical Exfoliation for Enhanced CO₂ Reduction Performance, *Angew. Chem. Int. Ed.* 57 (2018) 13283–13287.
- [33] B. Qin, Y. Li, Q. Zhang, G. Yang, H. Liang, F. Peng, Understanding of nitrogen fixation electro catalyzed by molybdenum–iron carbide through the experiment and theory, *Nano Energy* 68 (2020), 104374.
- [34] L. Gong, H. Yang, A.I. Douka, Y. Yan, B.Y. Xia, Recent Progress on NiFe-Based Electrocatalysts for Alkaline Oxygen Evolution, *Adv. Sust. Syst.* 5 (2020), 202000136.
- [35] M.W. Louie, A.T. Bell, An investigation of thin-film Ni-Fe oxide catalysts for the electrochemical evolution of oxygen, *J. Am. Chem. Soc.* 135 (2013) 12329–12337.
- [36] H. Xu, X. Li, W. Hu, Z. Yu, H. Zhou, Y. Zhu, L. Lu, C. Si, Research Progress of Highly Efficient Noble Metal Catalysts for the Oxidation of 5-Hydroxymethylfurfural, *ChemSusChem* 15 (2022), e202200352.
- [37] Y. Kwon, S.C.S. Lai, P. Rodriguez, M.T.M. Koper, Electrocatalytic Oxidation of Alcohols on Gold in Alkaline Media: Base or Gold Catalysis? *J. Am. Chem. Soc.* 133 (2011) 6914–6917.
- [38] B. Zhou, Y. Li, Y. Zou, W. Chen, W. Zhou, M. Song, Y. Wu, Y. Lu, J. Liu, Y. Wang, S. Wang, Platinum Modulates Redox Properties and 5-Hydroxymethylfurfural Adsorption Kinetics of Ni(OH)₂ for Biomass Upgrading, *Angew. Chem. Int. Ed.* 60 (2021) 22908–22914.
- [39] R. Luo, Y. Li, L. Xing, N. Wang, R. Zhong, Z. Qian, C. Du, G. Yin, Y. Wang, L. Du, A dynamic Ni(OH)₂-NiOOH/NiFeP heterojunction enabling high-performance E-upgrading of hydroxymethylfurfural, *Appl. Catal. B Environ.* 311 (2022), 121357.
- [40] W. Zhang, Y. Tang, L. Yu, X.-Y. Yu, Activating the alkaline hydrogen evolution performance of Mo-incorporated Ni(OH)₂ by plasma-induced heterostructure, *Appl. Catal. B Environ.* 260 (2020), 118154.
- [41] Y. Song, W. Xie, Y. Song, H. Li, S. Li, S. Jiang, J.Y. Lee, M. Shao, Bifunctional integrated electrode for high-efficient hydrogen production coupled with 5-hydroxymethylfurfural oxidation, *Appl. Catal. B Environ.* 312 (2022), 121400.
- [42] Y. Lu, T. Liu, C.L. Dong, C. Yang, L. Zhou, Y.C. Huang, Y. Li, B. Zhou, Y. Zou, S. Wang, Tailoring Competitive Adsorption Sites by Oxygen-Vacancy on Cobalt Oxides to Enhance the Electrooxidation of Biomass, *Adv. Mater.* 34 (2022), e2107185.
- [43] Y. Lu, C.-L. Dong, Y.-C. Huang, Y. Zou, Z. Liu, Y. Liu, Y. Li, N. He, J. Shi, S. Wang, Identifying the Geometric Site Dependence of Spinel Oxides for the Electrooxidation of 5-Hydroxymethylfurfural, *Angew. Chem. Int. Ed.* 59 (2020) 19215–19221.
- [44] Y. Wu, Y. Zhao, P. Zhai, C. Wang, J. Gao, L. Sun, J. Hou, Triggering Lattice Oxygen Activation of Single-Atomic Mo Sites Anchored on Ni-Fe Oxyhydroxides Nanoarrays for Electrochemical Water Oxidation, *Adv. Mater.* 34 (2022), 2202523.
- [45] Z.-F. Huang, S. Xi, J. Song, S. Dou, X. Li, Y. Du, C. Diao, Z.J. Xu, X. Wang, Tuning of lattice oxygen reactivity and scaling relation to construct better oxygen evolution electrocatalyst, *Nat. Commun.* 12 (2021) 3992.
- [46] X. Zheng, Y. Cao, Z. Wu, W. Ding, T. Xue, J. Wang, Z. Chen, X. Han, Y. Deng, W. Hu, Rational Design and Spontaneous Sulfurization of NiCo-(oxy) Hydroxysulfides Nanosheets with Modulated Local Electronic Configuration for Enhancing Oxygen Electrocatalysis, *Adv. Energy Mater.* 12 (2022), 202103275.